

# Terahertz Attoclock

YanJun Gao<sup>1,5</sup>, Yizhu Zhang<sup>3,\*</sup>, Yulin Chen<sup>4</sup>, Jingjing Zhao<sup>4</sup>, Meng Li<sup>2</sup>,  
Xiaokun Liu<sup>2</sup>, Yange Chen<sup>1,5</sup>, Jiahui Guo<sup>2</sup>, Ahai Chen<sup>2,†</sup> and Yuhai Jiang<sup>2,4,1‡</sup>

<sup>1</sup>Shanghai Advanced Research Institute, Chinese Academy of Sciences, Shanghai 201210, China

<sup>2</sup>Center for Transformative Science and School of Physical Science and Technology,  
ShanghaiTech University, Shanghai 201210, China

<sup>3</sup>School of Electrical Engineering, Tiangong University, Tianjin 300387, China

<sup>4</sup>School of Physics, Henan Normal University, Xinxiang 453007, China

<sup>5</sup>University of Chinese Academy of Sciences, Beijing 100049, China

(Dated: November 21, 2025)

The attoclock provides a powerful tool for studying ultrafast electron dynamics on the attosecond timescale. We demonstrate an all-optical terahertz (THz) attoclock that reconstructs electron dynamics during photoionization by detecting THz radiation emitted from gases ionized by the fundamental and second harmonic two-color laser fields, without the need for photoelectron detection. The polarization direction of the emitted THz field reflects the direction of the photoelectron drift velocity and thus encodes the effective delay. By measuring the THz waves from argon atoms ionized by the two-color fields, and by precisely controlling their relative phase and ellipticity, we observe intensity-dependent rotations of the THz polarization direction. Both experiment and time-dependent Schrödinger equation simulations reveal that the effective delay extracted from the THz polarization direction decreases with increasing laser intensity, consistent with conventional photoelectron attoclock results. Our experiment establishes the feasibility of the THz attoclock as a contactless probe of tunneling dynamics, with promising applications to condensed matter systems where photoelectron detection is impractical.

The photoelectron attoclock technique [1, 2] employs a nearly circularly polarized pulse to map the ionization time of an electron to its emission angle in the photoelectron momentum distribution (PMD), enabling attosecond time resolution. It has been applied to investigate tunneling time [1–9], tunneling geometry [10], and Coulomb effect [11], thereby advancing our understanding of strong-field ionization dynamics.

Recent studies have theoretically proposed a scheme for an optical attoclock in the terahertz regime (THz attoclock) [12, 13]. The THz attoclock circumvents the need for photoelectron detection by measuring the THz radiation induced by the acceleration of the photoelectron. The schematic of THz attoclock is illustrated in Fig. 1. A fundamental-frequency ( $\omega$ ) laser field (red waveform) and its second harmonic ( $2\omega$ , blue waveform) ionize argon atoms, and the resulting photoelectrons are subsequently accelerated in the combined  $\omega - 2\omega$  fields, leading to dipole radiation. Because the  $\omega - 2\omega$  fields are nearly circularly polarized, the electrons are driven far away from the parent ion. Consequently, the radiation does not come from high-harmonic generation via electron-ion recombination [14–16]. Instead, it originates from the transient acceleration of photoelectrons—known as Brunel radiation [17, 18]—which contributes to low-order harmonic generation. The lowest-frequency component of Brunel radiation corresponds to the THz emission [17, 18] (light-blue waveform in Fig. 1).

The connection between the THz emission and the PMD is illustrated in Fig. 1. The PMD represents the probability  $\mathcal{P}$  of photoelectrons with final velocity  $\mathbf{v}(t \rightarrow \infty)$ . Electrons accelerated in the asymmetric  $\omega - 2\omega$  fields produce an asymmetric PMD, whose asymmetry is defined as

$$\mathbf{P}_{\text{PMD}} = \mathbf{v}_{\text{int}}(t \rightarrow \infty) = \int_{\mathbf{v}} \mathcal{P}[\mathbf{v}(t \rightarrow \infty)] d\mathbf{v},$$

where  $\mathbf{v}_{\text{int}}$  denotes integrated velocity of the emitted photoelectrons. The asymmetric direction of PMD  $\hat{\mathbf{P}}_{\text{PMD}}$  is indicated as the red arrow in Fig. 1. The Brunel harmonic radiation originates from the transient acceleration of photoelectrons, expressed as

$$\mathbf{E}_{\text{Brunel}}(t) \propto \frac{\partial \mathbf{v}_{\text{int}}(t)}{\partial t}.$$

Its lowest-frequency component corresponds to the THz emission and can be expressed as

$$\mathbf{E}_{\text{THz}} \propto \lim_{\nu \rightarrow 0} \int_{-\infty}^{\infty} \frac{\partial \mathbf{v}_{\text{int}}(t)}{\partial t} e^{-i2\pi\nu t} dt = \mathbf{v}_{\text{int}}(t \rightarrow \infty).$$

By controlling the relative phase  $\varphi$  of  $\omega - 2\omega$  fields, the asymmetric fields induce a non-zero  $\mathbf{v}_{\text{int}}(t \rightarrow \infty)$ , i.e., a residual photocurrent [19, 20], which gives rise to the THz radiation. Evidently, the polarization direction of the THz field,  $\hat{\mathbf{E}}_{\text{THz}}$  (blue arrow in Fig. 1), coinciding with  $\hat{\mathbf{P}}_{\text{PMD}}$ , is consistent with the direction of  $\mathbf{v}_{\text{int}}(t \rightarrow \infty)$ . In a conventional photoelectron attoclock, the tunneling time delay is encoded in the angular deflection of  $\hat{\mathbf{P}}_{\text{PMD}}$ . Since  $\hat{\mathbf{E}}_{\text{THz}}$  is equivalent to  $\hat{\mathbf{P}}_{\text{PMD}}$ ,  $\hat{\mathbf{E}}_{\text{THz}}$  can therefore serve as an all-optical proxy for reconstructing the tunneling delay of photoelectrons.

\* zhangyizhu@tiangong.edu.cn

† chenah1@shanghaitech.edu.cn

‡ jiangyh3@shanghaitech.edu.cn

Although the THz polarization has been previously employed to probe photoelectron dynamics [13, 21–24], the experimental realization of the THz attoclock remains challenging. The first difficulty is technical: the relative phase  $\varphi$  between the  $\omega$  and  $2\omega$  fields must be precisely controlled and calibrated at different laser intensities, so that the subtle angular deflection of  $\hat{\mathbf{E}}_{\text{THz}}$  can be accurately compared. A second challenge lies in the independent control of the field ellipticity, since large ellipticity suppresses electron–ion recollision, which would otherwise complicate the THz attoclock measurement [13]. Furthermore, THz generation in the  $\omega - 2\omega$  scheme involves multiple coupled processes, including photoionization, nonlinear self-focusing and defocusing, and THz absorption losses in plasma [25–30]. Hence, whether the THz attoclock can effectively isolate electron dynamics from these intertwined processes still requires experimental verification.

In this Letter, we demonstrate the first successful implementation of the THz attoclock. An actively phase-stable Mach–Zehnder (M-Z) interferometer is employed to stabilize and control the relative phase  $\varphi$ , which is calibrated using time-dependent Schrödinger equation (TDSE) simulations. The ellipticity of the  $\omega - 2\omega$  fields is carefully optimized to suppress electron–ion recombination. Our measurements reveal that the rotation of  $\hat{\mathbf{E}}_{\text{THz}}$  at fixed  $\varphi$  corresponds to a decreasing effective delay with increasing laser intensity, in agreement with TDSE simulations and previous photoelectron attoclock experiments. These results establish the feasibility of the THz attoclock as a non-vacuum, all-optical, and non-contact approach to probing ultrafast electron dynamics.

In our experimental setup for the THz attoclock (see Supplementary Section I for details), two-color ( $\omega - 2\omega$ ) co-rotating fields are implemented [30–32], ensuring high THz radiation efficiency. The  $\omega$  field (810 nm, 60 fs, 1 kHz) is derived from a Ti:sapphire laser system. The  $2\omega$  field is generated by frequency-doubling the fundamental pulse via a  $\beta$ -barium-borate (BBO) crystal. The two-color fields are split into two arms of the M-Z interferometer via a dichroic mirror, thus enabling independent control of the intensity and polarization states of the two fields. A  $\lambda/2$  wave plate and a  $\lambda/4$  wave plate are placed in each beam so that the ellipticities of the  $\omega$  and  $2\omega$  fields can be adjusted to  $\epsilon_\omega \approx 0.81$  and  $\epsilon_{2\omega} \approx 0.97$ , respectively (see Supplementary Section II for the calibration of ellipticity). The major axis of the  $\omega$  field is along the  $y$  axis. The relative phase  $\varphi$  between the  $\omega - 2\omega$  fields is finely adjusted by changing the distance between the BBO and the plasma [33, 34]. To suppress phase jitter between the  $\omega - 2\omega$  beams, we minimize both the optical path length and the number of reflecting mirrors in the M-Z interferometer. Additionally, an active phase-stable system is implemented to stabilize relative phase fluctuations below  $\pm 0.02\pi$ . The phase fluctuations are presented in Supplementary Section IV. By maintaining the peak intensity ratio between the  $\omega$  field and  $2\omega$  field at 3:1, both laser beams are focused collinearly into

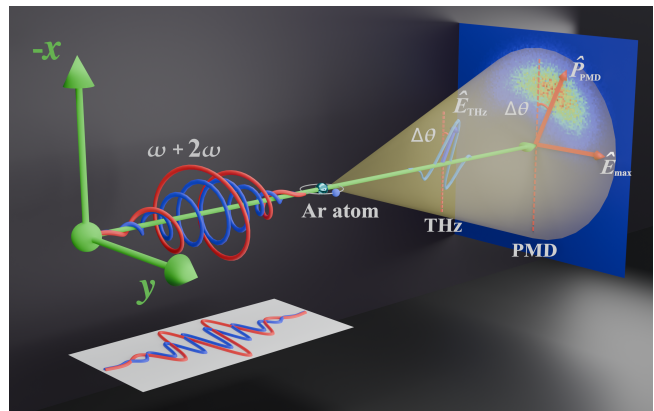


FIG. 1. Schematic of THz attoclock. A fundamental field with an ellipticity of  $\epsilon_\omega \approx 0.81$  and its major axis direction along the  $y$  axis, together with a circularly polarized second harmonic field ( $\varphi = 0$ ), jointly ionize Ar atoms. The ionized photoelectrons are accelerated and radiate THz waves under the action of the two-color fields. Because the drift velocity of tunneling electrons accelerated in the two-color fields determines the magnitude and direction of the radiated THz field, the THz polarization direction ( $\hat{\mathbf{E}}_{\text{THz}}$ ) aligns with the asymmetric direction of the PMD ( $\hat{\mathbf{P}}_{\text{PMD}}$ ). Equivalent to photoelectron attoclock, the time when electrons appear in the continuous state can also be mapped to the deflection of  $\hat{\mathbf{E}}_{\text{THz}}$ . The angular offset  $\Delta\theta$  refers to the angle between  $\hat{\mathbf{E}}_{\text{THz}}$  (or  $\hat{\mathbf{P}}_{\text{PMD}}$ ) and the minor axis of the  $\omega$  field, which can be mapped to the effective delay in tunneling ionization.  $\hat{\mathbf{E}}_{\text{max}}$  refers to the direction at the peak of the total electric field.

the argon gas cell, with coincident focal points, inducing plasma formation and nearly linearly polarized THz wave emission [35].  $I$  is defined as the sum of the peak intensities of the two-color fields,  $I = I_\omega + I_{2\omega}$ , where  $I_\omega$  and  $I_{2\omega}$  represent the peak intensities of the  $\omega$  and  $2\omega$  fields, respectively. The peak electric fields along two orthogonal polarization directions of THz radiation ( $E_x$ ,  $E_y$ ) are measured using the electro-optic sampling (EOS) method with a ZnTe crystal, thereby obtaining the THz polarization direction. The ZnTe crystal is calibrated to have the same response to  $E_x$  and  $E_y$  (see Supplementary Section III for details).

In implementing the THz attoclock, it is essential to accurately determine the relative phase  $\varphi$  between the  $\omega$  and  $2\omega$  fields. The polarization direction of the THz field,  $\hat{\mathbf{E}}_{\text{THz}}$ , generated by circularly or elliptically polarized  $\omega - 2\omega$  fields, rotates as  $\varphi$  varies [35]. For reliable THz attoclock measurements, the dependence of  $\hat{\mathbf{E}}_{\text{THz}}$  on laser intensity must therefore be compared at a fixed  $\varphi$ . However, precisely defining and maintaining the absolute value of  $\varphi$  in experiment is technically challenging. The intensity adjustments can introduce phase jitter, and such minor variations in  $\varphi$  can lead to pronounced changes in  $\hat{\mathbf{E}}_{\text{THz}}$ , thereby affecting the accuracy of THz attoclock measurements. Figs. 2(a) and 2(d) show the THz peak electric fields in the hor-

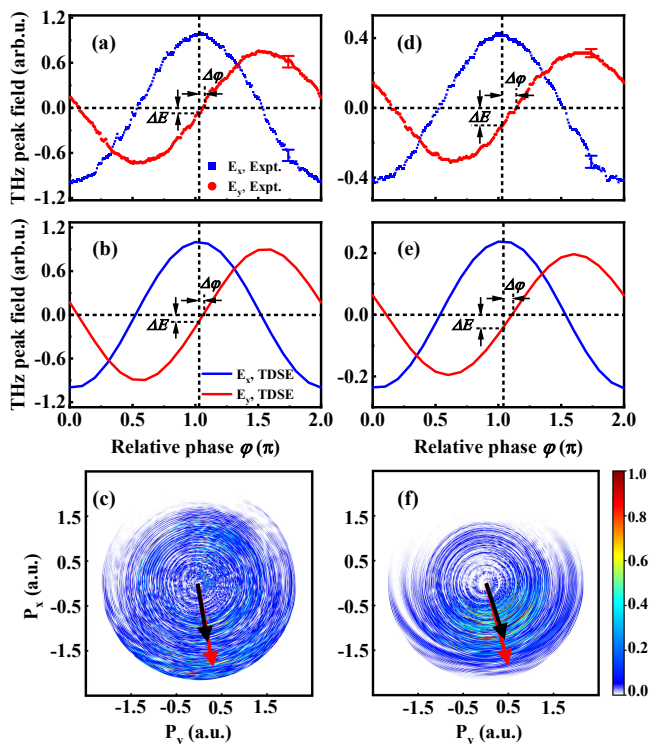


FIG. 2. THz yield at different laser intensities  $I$ . (a,b) Measured and TDSE-calculated THz peak electric fields along the horizontal and vertical polarizations as a function of the relative phase of the two-color fields,  $E_x(\varphi)$  (blue) and  $E_y(\varphi)$  (red), at  $I = 2.9 \times 10^{14} \text{ W/cm}^2$ . The  $\varphi$  axis is calibrated.  $\Delta\varphi$  is defined as the phase difference between the  $\varphi$  at the maximum of  $E_x$  and that where  $E_y = 0$ .  $\Delta E$  denotes the absolute value of  $E_y$  at the maximum of  $E_x$ . (c) TDSE-calculated PMD, along with the TDSE-calculated  $\hat{\mathbf{E}}_{\text{THz}}$  (red arrow) and measured THz polarization direction  $\hat{\mathbf{E}}_{\text{THz}}$  (black arrow) at  $\varphi = 0$  and  $I = 2.9 \times 10^{14} \text{ W/cm}^2$ . (d,e) Same as (a,b), but for  $I = 1.6 \times 10^{14} \text{ W/cm}^2$ . Error bars in (a) and (d) represent the standard deviation. (f) Same as (c), but for  $I = 1.6 \times 10^{14} \text{ W/cm}^2$ .

horizontal and vertical directions as a function of  $\varphi$  at the different intensities. Fig. 2(a) presents  $E_x(\varphi)$  and  $E_y(\varphi)$  at  $I = 2.9 \times 10^{14} \text{ W/cm}^2$ , while Fig. 2(d) shows the corresponding results at  $I = 1.6 \times 10^{14} \text{ W/cm}^2$ . Within each panel, the data points of  $E_x(\varphi)$  and  $E_y(\varphi)$  (blue and red dots) are phase-stable and aligned along the same phase axis  $\varphi$ , enabling direct comparison. However, varying the laser intensity can cause slight fluctuations in  $\varphi$ . Without phase calibration, the  $\varphi$  axes in Figs. 2(a) and 2(d) differ, making direct comparison between datasets impossible. Moreover, without an accurate determination of  $\varphi$ , the directions of the vector potentials of the  $\omega$  and  $2\omega$  fields remain undefined, and the resulting angular offset cannot be determined.

We calibrate  $\varphi$  according to TDSE simulations based on the well-established Qprop library [36]. The simulations are performed with a maximum orbital angular

momentum of up to 100 in the partial-wave expansion to ensure convergence (see Supplementary). The results show that as the total intensity  $I$  of the two-color fields decreases from  $4 \times 10^{14}$  to  $1 \times 10^{14} \text{ W/cm}^2$ , the phase at which  $E_x$  is maximized lies in the range of  $1.02\pi$  to  $1.04\pi$  (see Supplementary Section V). We therefore assign the phase of maximum  $E_x$  to the mean value of  $1.03\pi$ . The associated calibration uncertainty is about  $0.01\pi$ , comparable to the intrinsic phase jitter of the actively phase-stable two-color M-Z interferometer.

In Figs. 2(a) and 2(d),  $E_x(\varphi)$  and  $E_y(\varphi)$  at different intensities  $I$  are plotted along the calibrated  $\varphi$  axis for direct comparison. Both experiment (Figs. 2(a), 2(d)) and TDSE simulations (Figs. 2(b), 2(e)) show that  $E_x$  and  $E_y$  increase with  $I$ . As  $I$  decreases,  $E_y(\varphi)$  exhibits a relative phase shift with respect to  $E_x(\varphi)$ , quantified by  $\Delta\varphi$  and  $\Delta E$  (Fig. 2). As  $I$  decreases,  $\Delta\varphi$  and  $\Delta E$  increase, consistent with TDSE results. Since the THz polarization angle is given by  $\theta = \arctan(E_y/E_x)$ , variations in  $\Delta\varphi$  and  $\Delta E$  at different  $I$  directly correspond to a rotation of  $\hat{\mathbf{E}}_{\text{THz}}$ . Figs. 2(c) and 2(f) show the measured and simulated  $\hat{\mathbf{E}}_{\text{THz}}$  at different  $I$ . The theoretical PMD and  $\hat{\mathbf{E}}_{\text{THz}}$  are obtained via TDSE simulation for hydrogen atom.

It should be noted that in the photocurrent model, both  $\Delta\varphi$  and  $\Delta E$  vanish, corresponding to a fixed phase difference of  $0.5\pi$  between  $E_y(\varphi)$  and  $E_x(\varphi)$ , independent of the laser intensity  $I$ . According to this model,  $\hat{\mathbf{E}}_{\text{THz}}$  remains horizontally at  $\varphi = 0$ , independent of  $I$  (see Supplementary Sect. VI). In contrast, nonzero and intensity-dependent  $\Delta\varphi$  and  $\Delta E$  can only be reproduced by TDSE and classical trajectory Monte Carlo (CTMC) simulations [37–39], where the Coulomb potential is included. Experimentally, we observe finite and intensity-varying  $\Delta\varphi$  and  $\Delta E$ , providing direct evidence that the THz attoclock successfully probes photoelectron dynamics.

Fig. 3 presents the angular offset  $\Delta\theta$  as a function of the calibrated laser intensity  $I$ , where  $\Delta\theta$  denotes the angle between  $\hat{\mathbf{E}}_{\text{THz}}$  and the minor axis of the  $\omega$  field. The effective delay  $\tau$  is extracted using  $\Delta\theta \approx 1.44\omega\tau$  [12], where  $\tau$  does not represent a physical tunneling delay [12]. Because the peak intensity  $I$  at focus cannot be measured directly,  $I$  is calculated from the pulse energy and the estimated beam waist radii. Using the wavelengths, focal lengths, and pre-focus spot sizes, the waists of the  $\omega$  and  $2\omega$  fields are estimated as  $50 \mu\text{m}$  and  $25 \mu\text{m}$ , respectively, allowing calibration of  $I$  via  $I = I_\omega + I_{2\omega}$  and direct comparison with hydrogen TDSE simulations (black triangles). We further compare the THz attoclock with the single-color photoelectron attoclock in Ar [10] (blue squares). Since the latter employs an elliptically polarized field, its PMD angular offset cannot be directly matched to the THz polarization angle. The PMD angular offset  $\Delta\theta'$  is converted to the effective delay  $\tau$  as  $\Delta\theta' \approx 1.28\omega\tau$  [12], enabling a consistent comparison between the two techniques. The effective delay  $\tau$  obtained from the THz attoclock decreases with increasing inten-

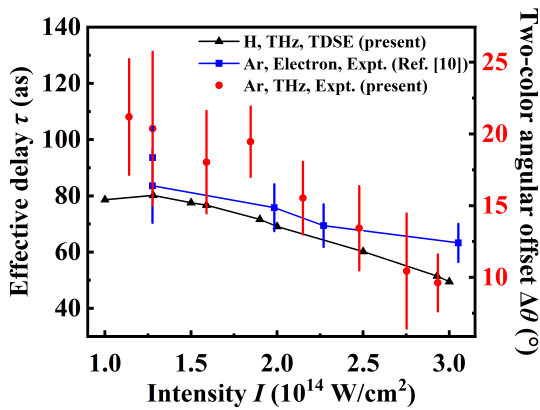


FIG. 3.

Comparison of the experimental and TDSE results for the THz attoclock, together with experimental data from the photoelectron attoclock. Red dots show the measured angular offset  $\Delta\theta$  of the THz polarization and the corresponding effective delay  $\tau$  in Ar as a function of the laser peak intensity  $I$  at the  $\omega - 2\omega$  phase  $\varphi = 0$ , with error bars indicating standard deviations. Black triangles denote TDSE simulations of the THz attoclock for hydrogen atom. Blue squares display the effective delay  $\tau$  extracted from the single-color photoelectron attoclock in Ar.

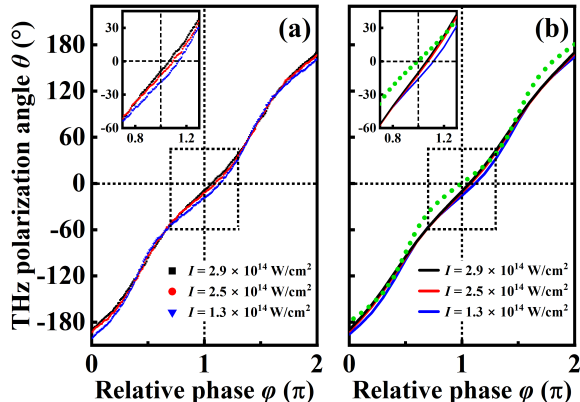


FIG. 4. Polarization angle  $\theta$  of the THz field  $\hat{\mathbf{E}}_{\text{THz}}$  as a function of the two-color relative phase  $\varphi$  for different laser intensities  $I$ . (a) Experimental results for Ar. (b) TDSE and photocurrent simulations. The solid curves show the TDSE results. The green dotted curve shows the photocurrent prediction at a laser intensity of  $1.3 \times 10^{14} \text{ W/cm}^2$ .

sity  $I$ , consistent with the trend observed in the single-color photoelectron attoclock [10], which confirms the robustness of the THz attoclock method.

While Fig. 3 examines the variation of  $\hat{\mathbf{E}}_{\text{THz}}$  with laser intensity  $I$  at the fixed  $\omega - 2\omega$  phase  $\varphi = 0$ , Fig. 4 extends the analysis to the full range of  $\varphi$  from 0 to  $2\pi$ . Figs. 4(a) and (b) show the measured and TDSE-calculated angle  $\theta$  of  $\hat{\mathbf{E}}_{\text{THz}}$  as a function of  $\varphi$  for different  $I$ . The green dotted line represents the photocurrent model, which neglects the Coulomb potential and predicts  $\theta = 0$  at  $\varphi = \pi$ . In contrast, TDSE simulations that include the Coulomb interaction exhibit a zero crossing of the  $\varphi$ - $\theta$  curves shifted to  $\varphi > \pi$ . As  $I$  increases, the electron escapes more rapidly, reducing the Coulomb influence and causing the  $\varphi$ - $\theta$  curves to converge toward the photocurrent prediction. The close agreement between experiment and TDSE validates the robustness of our measurements. Owing to the equivalence between  $\hat{\mathbf{E}}_{\text{THz}}$  and  $\hat{\mathbf{P}}_{\text{PMD}}$ , the  $\varphi$ - $\theta$  dependence connects the phase-of-phase curve in PMDs [8], offering a pathway to reconstruct tunneling dynamics in future work.

In summary, we demonstrate the feasibility of the THz attoclock for probing strong-field electron dynamics. By measuring the orthogonal THz yields  $E_x(\varphi)$  and  $E_y(\varphi)$ , the relative phase  $\varphi$  is self-calibrated, enabling direct comparison of the THz polarization direction  $\hat{\mathbf{E}}_{\text{THz}}$  across different laser intensities  $I$ . The extracted effective delay  $\tau$  decreases with increasing  $I$ , consistent with TDSE simulations and photoelectron attoclock measurements. The measured  $\varphi$ - $\theta$  dependence also converges toward the classical photoelectron prediction at higher intensities, further confirming the robustness of the method. These results establish the all-optical THz attoclock as a vacuum-free, contactless probe of tunneling electron motion, offering a promising route toward studying tunneling dynamics in condensed-matter systems.

## ACKNOWLEDGMENTS

We acknowledge financial support from the National Key Research and Development Program of China (No. 2022YFA1604302), the National Natural Science Foundation of China (Nos. 12334011, 12374262 and 12174284), and the Natural Science Foundation of Henan (Grant No. 252300421304).

[1] P. Eckle, M. Smolarski, P. Schlup, J. Biegert, A. Staudte, M. Schöffler, H. G. Müller, R. Dörner, and U. Keller, Attosecond angular streaking, *Nat. Phys.* **4**, 565 (2008).  
 [2] P. Eckle, A. N. Pfeiffer, C. Cirelli, A. Staudte, R. Dörner, H. G. Müller, M. Büttiker, and U. Keller, Attosecond ionization and tunneling delay time measurements in helium, *Science* **322**, 1525 (2008).

[3] A. S. Landsman, M. Weger, J. Maurer, R. Boge, A. Ludwig, S. Heuser, C. Cirelli, L. Gallmann, and U. Keller, Ultrafast resolution of tunneling delay time, *Optica* **1**, 343 (2014).  
 [4] L. Torlina, F. Morales, J. Kaushal, I. Ivanov, A. Kheifets, A. Zielinski, A. Scrinzi, H. G. Müller, S. Sukiasyan, M. Ivanov, and O. Smirnova, Interpreting attoclock mea-

- surements of tunnelling times, *Nature Physics* **11**, 503 (2015).
- [5] N. Camus, E. Yakaboylu, L. Fechner, M. Klaiber, M. Laux, Y. Mi, K. Z. Hatsagortsyan, T. Pfeifer, C. H. Keitel, and R. Moshhammer, Experimental evidence for quantum tunneling time, *Phys. Rev. Lett.* **119**, 023201 (2017).
- [6] U. S. Sainadh, H. Xu, X. Wang, A. Atia-Tul-Noor, W. C. Wallace, N. Douguet, A. Bray, I. Ivanov, K. Bartschat, A. Kheifets, *et al.*, Attosecond angular streaking and tunnelling time in atomic hydrogen, *Nature* **568**, 75 (2019).
- [7] A. S. Kheifets, The attoclock and the tunneling time debate, *Journal of Physics B: Atomic, Molecular and Optical Physics* **53**, 072001 (2020).
- [8] M. Han, P. Ge, J. Wang, Z. Guo, Y. Fang, X. Ma, X. Yu, Y. Deng, H. J. Wörner, Q. Gong, and Y. Liu, Complete characterization of sub-coulomb-barrier tunnelling with phase-of-phase attoclock, *Nature Photonics* **15**, 765 (2021).
- [9] C. Hofmann, A. Bray, W. Koch, H. Ni, and N. I. Shvetsov-Shilovski, Quantum battles in attoscience: tunnelling, *The European Physical Journal D* **75**, 208 (2021).
- [10] A. N. Pfeiffer, C. Cirelli, M. Smolarski, D. Dimitrovski, M. Abu-Samaha, L. B. Madsen, and U. Keller, Attoclock reveals natural coordinates of the laser-induced tunnelling current flow in atoms, *Nat. Phys.* **8**, 76 (2012).
- [11] X. Li, X. Liu, C. Wang, S. Ben, S. Zhou, Y. Yang, X. Song, J. Chen, W. Yang, and D. Ding, Coulomb focusing in attosecond angular streaking, *Light: Science & Applications* **13**, 250 (2024).
- [12] I. Babushkin, Á. J. Galán, J. R. C. de Andrade, A. Husakou, F. Morales, M. Kretschmar, T. Nagy, V. Vaičaitis, L. Shi, D. Zuber, *et al.*, All-optical attoclock for imaging tunnelling wavepackets, *Nat. Phys.* **18**, 417 (2022).
- [13] Z. Gan, K. Zhang, Y. Gao, A. Chen, Y. Zhang, T.-M. Yan, T. Pfeifer, and Y. Jiang, Probing electronic motion and core potential by coulomb-reshaped terahertz radiation, *Phys. Rev. A* **110**, 013110 (2024).
- [14] A. McPherson, G. Gibson, H. Jara, U. Johann, T. S. Luk, I. McIntyre, K. Boyer, and C. K. Rhodes, Studies of multiphoton production of vacuum-ultraviolet radiation in the rare gases, *Journal of the Optical Society of America B* **4**, 595 (1987).
- [15] M. Lewenstein, P. Balcou, M. Y. Ivanov, A. L’huillier, and P. B. Corkum, Theory of high-harmonic generation by low-frequency laser fields, *Physical Review A* **49**, 2117 (1994).
- [16] P.-M. Paul, E. S. Toma, P. Breger, G. Mullot, F. Augé, P. Balcou, H. G. Muller, and P. Agostini, Observation of a train of attosecond pulses from high harmonic generation, *Science* **292**, 1689 (2001).
- [17] F. Brunel, Harmonic generation due to plasma effects in a gas undergoing multiphoton ionization in the high-intensity limit, *J. Opt. Soc. Am. B* **7**, 521 (1990).
- [18] I. Babushkin, C. Brée, C. M. Dietrich, A. Demircan, U. Morgner, and A. Husakou, Terahertz and higher-order brunel harmonics: from tunnel to multiphoton ionization regime in tailored fields, *J. Mod. Opt.* **64**, 1078 (2017).
- [19] K.-Y. Kim, J. H. Glowonia, A. J. Taylor, and G. Rodriguez, Terahertz emission from ultrafast ionizing air in symmetry-broken laser fields, *Opt. Express* **15**, 4577 (2007).
- [20] K.-Y. Kim, A. J. Taylor, J. Glowonia, and G. Rodriguez, Coherent control of terahertz supercontinuum generation in ultrafast laser–gas interactions, *Nat. photonics* **2**, 605 (2008).
- [21] K. Zhang, Y. Zhang, X. Wang, Z. Shen, T.-M. Yan, and Y. Jiang, Experimental evidence for terahertz emission of continuum electrons in the dual-color laser field, *Opt. Lett.* **45**, 1838 (2020).
- [22] K. Zhang, Y. Zhang, X. Wang, T.-M. Yan, and Y. Jiang, Continuum electron giving birth to terahertz emission, *Photon. Res.* **8**, 760 (2020).
- [23] Y. Gao, Y. Zhang, K. Zhang, Z. Gan, T.-M. Yan, and Y. Jiang, Coulomb potential determining terahertz polarization in a two-color laser field, *Opt. Lett.* **48**, 2575 (2023).
- [24] Z. Gan, A. Chen, J. Guo, Y. Chen, T.-M. Yan, Y. Zhang, and Y. Jiang, Characterizing strong-field tunneling ionization with a phase-dependent thz polarization spectrum, *Opt. Express* **32**, 33552 (2024).
- [25] C. Jin, A.-T. Le, and C. Lin, Medium propagation effects in high-order harmonic generation of ar and n 2, *Phys. Rev. A* **83**, 023411 (2011).
- [26] L. Bergé, S. Skupin, C. Köhler, I. Babushkin, and J. Herrmann, 3d numerical simulations of thz generation by two-color laser filaments, *Phys. Rev. Lett.* **110**, 073901 (2013).
- [27] E. Esarey, P. Sprangle, J. Krall, and A. Ting, Self-focusing and guiding of short laser pulses in ionizing gases and plasmas, *IEEE J. Quantum Electron.* **33**, 1879 (2002).
- [28] A. Couairon and A. Mysyrowicz, Femtosecond filamentation in transparent media, *Phys. Rep.* **441**, 47 (2007).
- [29] L. Bergé, S. Skupin, R. Nuter, J. Kasparian, and J.-P. Wolf, Ultrashort filaments of light in weakly ionized, optically transparent media, *Rep. Prog. Phys.* **70**, 1633 (2007).
- [30] Y. Zhang, Z.-H. Jiao, T. He, J. Zhao, X. Fan, T. Chen, G.-L. Wang, T.-M. Yan, X.-X. Zhou, and Y. Jiang, Intensity-surged and bandwidth-extended terahertz radiation in two-foci cascading plasmas, *Optics Letters* **47**, 3816 (2022).
- [31] J. Zhao, Y. Zhang, Y. Gao, M. Li, X. Liu, W. Liu, T.-M. Yan, and Y. Jiang, Temporal-spatial manipulation of bi-focal bi-chromatic fields for terahertz radiations, *Communications Physics* **7**, 408 (2024).
- [32] J. Zhao, Y. Zhang, Y. Gao, A. Chen, and Y. Jiang, Two-color strong-field terahertz amplification in the non-identical focusing condition, *Applied Physics Letters* **126** (2025).
- [33] M. Kress, T. Löffler, S. Eden, M. Thomson, and H. G. Roskos, Terahertz-pulse generation by photoionization of air with laser pulses composed of both fundamental and second-harmonic waves, *Opt. Lett.* **29**, 1120 (2004).
- [34] H. Wen and A. M. Lindenberg, Coherent terahertz polarization control through manipulation of electron trajectories, *Phys. Rev. Lett.* **103**, 023902 (2009).
- [35] J. Dai, N. Karpowicz, and X.-C. Zhang, Coherent polarization control of terahertz waves generated from two-color laser-induced gas plasma, *Phys. Rev. Lett.* **103**, 023001 (2009).
- [36] V. Tulskey and D. Bauer, Qprop with faster calculation of photoelectron spectra, *Computer Physics Communications* **251**, 107098 (2020).
- [37] J. Liu, W. Chen, B. Zhang, J. Zhao, J. Wu, J. Yuan, and

- Z. Zhao, Trajectory-based analysis of low-energy electrons and photocurrents generated in strong-field ionization, *Phys. Rev. A* **90**, 063420 (2014).
- [38] J. Liu, Y. Fu, W. Chen, Z. Lü, J. Zhao, J. Yuan, and Z. Zhao, Offset angles of photocurrents generated in few-cycle circularly polarized laser fields, *J. Phys. B: At. Mol. Opt. Phys.* **50**, 055602 (2017).
- [39] J. Liu, J. Zhao, Y. Huang, X. Wang, and Z. Zhao, Dynamics of rydberg states and terahertz waves generated in strong few-cycle laser pulses, *Phys. Rev. A* **102**, 023109 (2020).